Effects of the state of boron on the proton-boron fusion reaction

Xiaochuan Ning[1,4], Tianyi Liang[1,4], Dong Wu[2,5], Shujun Liu[1], Yangchun Liu[1], Zhengmao Sheng[1,5], Jieru Ren[3], Bowen Jiang[3], Yongtao Zhao[3], Dieter H. H. Hoffmann[3], and X. T. He[1]

[1] *Institute for Fusion Theory and Simulation, Department of Physics, Zhejiang University, Hangzhou 310027, China*

[2] *Key Laboratory for Laser Plasmas and School of Physics and Astronomy, and Collaborative Innovation Center of IFSA (CICIFSA), Shanghai Jiao Tong University, Shanghai 200240, China*

[3] *MOE Key Laboratory for Nonequilibrium Synthesis and Modulation of Condensed Matter, School of Physics, Xian Jiaotong University, Xian 710049, China.*

[4] These authors contributed equally: X. C. Ning, T. Y. Liang.

[5] Correspondence and requests for materials should be addressed to D. Wu (email: dwu.phys@sjtu.edu.cn) or to Z. M. Sheng (email: zmsheng@zju.edu.cn).

Abstract

It becomes increasingly attractive to use intense laser beams or intense laser-accelerated proton beams to impact a boron target so as to generate the $p^{11}B$ reaction and produce α particles. Labaune *et al* [Nat. Commun. 4: 2506, 2013] first experimentally found that the state of a boron target (solid or plasma) played an important role in the $p^{11}B$ fusion reaction. Considering the inner physical mechanism is still not clear, we have recently performed a set of simulations on the laser-boron interaction and the $p^{11}B$ fusion reaction. It is found that degeneracy effects and collective electromagnetic effects will exert influences on the number of fusion reactions through changing the energy loss of proton beams. To be more specific, we find that the collective electromagnetic effects play the dominant role in the $p^{11}B$ fusion reaction and the yields of α particles, and the degeneracy effects play a secondary role. Our results may be able to serve as a reference for not only analyzing or improving further experiments of the $p^{11}B$ fusion reaction, but also investigating other beam-plasma systems such as ion-driven inertial confinement fusion and fast ignition.

There is definitely progress in fusion experiments towards the final goal to contribute to the world energy supply even though this progress is slow. Both the magnetical confinement fusion experiments and the inertial confinement fusion experiments have achieved significant milestones in these years. The Experimental Advanced Superconducting Tokomak (EAST) at Hefei have made a world record for realizing a 101-second H-mode discharge [1], and the most advanced experiments at the Livermore National Ignition Facility (NIF) have obtained a 1.35-MJ fusion energy output recently, which is about 70% of the laser input energy [2]. Despite the great achievements, there remains a long way to go to solve the energy problem. For the magnetic confinement approach, adequate plasma confinement time and qualified materials that can bear the tough conditions in the inner modules of the reactor are still two main issues to be addressed. As for the inertial confinement approach, in the case of the NIF, though it obtains a 1.35-MJ energy, it starts with more than 400 MJ of stored energy. From this perspective, the ratio of the total output energy to the total input energy is quite low and far from the envisioned goal to achieve a gain of 10. Moreover, 14-MeV neutrons produced by the deuterium-tritium fusion also raise some concern about induced radioactivity and it is still a challenging problem to efficiently convert the neutron energy into useful electricity.

While we are convinced that nuclear fusion is the world energy source of the future, it is obvious that even if from now on all fusion scenarios based on ITER technology or similar, proceed on schedule, fusion will not contribute significantly to eliminate the problems associated with climate change during this century. Having said that, we believe that it makes sense to investigate fusion scenarios that use fusion fuel which is not radioactive, and is available in abundant quantities. The holy grail of advanced fusion fuels therefore is considered to be the $p^{11}B$ reaction, where the primary reaction produces 3 energetic α particles. Only secondary reactions are producing neutrons, and induced radioactivity. Due to the lower cross section as compared to D-T fusion and a much higher ignition temperature, energy gain from proton-boron fusion is much more difficult to achieve.

Nevertheless, due to advances in laser technology, the $p^{11}B$ fusion has drawn renewed attention. The proposal of using intense laser beams or intense laser-accelerated proton beams to impact a boron target so as to generate the $p^{11}B$ fusion is becoming increasingly attractive. Based on this method, a number of groups [3, 4, 5, 6, 7, 8, 9] have performed a series of experiments on the $p^{11}B$ fusion reaction and measured the yields of α particles. Meanwhile, much significant progress has also continuously been made in this field. The record yield of α particles has been increased from about 10^5/sr in 2005 [3, 10] to about 10^{10}/sr in 2020 [7]. However, there still remain unclear physical problems in the interaction of intense proton beams and a boron target, which strongly depends on the intensity of proton beams as well as the conditions of the boron target including temperature, density, ingredients and so on, and potentially has a large influence on the chances of the $p^{11}B$ fusion reaction and the α-particle yields. Labaune *et al* [4] first experimentally found that the state of a boron target (solid or plasma) played an important role in the $p^{11}B$ fusion reaction. In their experiments, compared with a normal boron solid, a laser-ablated boron solid (boron plasma) can produce much more α particles under the impact of proton beams accelerated by a picosecond laser. In order to figure out this problem, we have recently performed a set of simulations according to the experiments.

1 Results

1.1 The interaction between a nanosecond laser and a boron solid

First, to ascertain the specific state of the boron target after ablated, we have performed a one-dimensional radiation-hydrodynamic simulation with the MULTI-1D code [11] on the interaction of a nanosecond laser pulse and a boron solid, which is the first step in the experiment of Labaune *et al.* The grid size is 8 μm and the time step is 0.02 ns. To be consistent with the experiments, the laser duration time is 1.5 ns with a 0.53 μm wavelength and an intensity of 6×10^{14} Wcm^{-2}. The results are displayed in Fig. 1. It can be seen that under ablation of the laser, the boron target spread outwards and the temperature rises. We have extracted the data at t=1.2 ns, as shown in Fig. 1 (b) and (d). A low-density boron plasma is widely formed in the region away from the boron solid, whereas on the surface of the boron solid, there is actually a high-density boron plasma, which, to the best of our knowledge, was not considered seriously. We note that the surface boron plasma is about 5 times denser than the boron solid and its range is about tens of microns. Meanwhile, its temperature is about 10 eV. It is worth mentioning that after the laser ablated the boron solid, degeneracy effects indeed should be taken into account with such parameters.

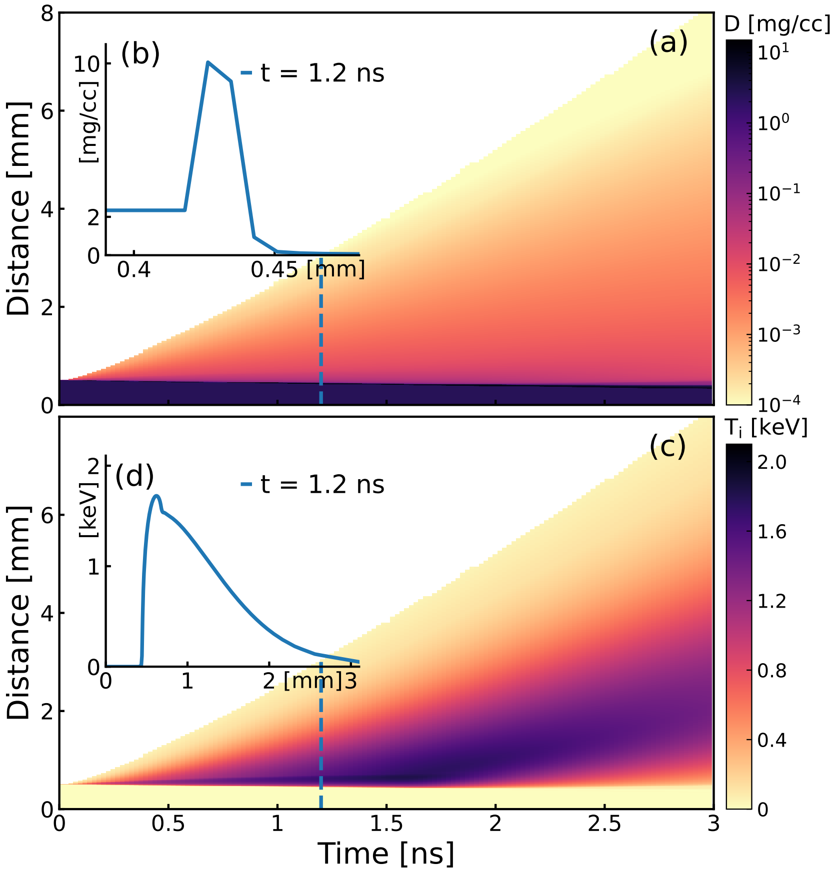

Fig. 1: Evolution of the mass density distribution in (a) and the temperature distribution in (c) of boron ions with time. (b) and (d) correspond to the mass density distribution and the temperature distribution at t=1.2 ns, respectively

1.2 The interaction between an intense proton beam and boron targets with different states

With the calculated target conditions, we have further performed another set of two-dimensional simulations with the LAPINS code [12, 13, 14, 15, 16] on the p^{11}B fusion by injecting an intense proton beam into a boron target. In the LAPINS model, plasma ions and the injected beam particles are treated by the traditional PIC method, while plasma electrons are treated as a fluid, of which the current density is solved by the Ampere's law, $\mathbf{J}_e = (1/2\pi)\nabla \times$

$\mathbf{B} - (1/2\pi)(\partial \mathbf{E}/\partial t) - \mathbf{J}_b - \mathbf{J}_i$, where $\mathbf{B}$ is the magnetic field, $\mathbf{E}$ is the electric field, $\mathbf{J}_b$ is the beam current density and $\mathbf{J}_i$ is the plasma ion current density. The electric field is obtained by the Ohm's law, $\mathbf{E} = \eta \mathbf{J}_e - \mathbf{v}_e \times \mathbf{B} - \nabla p_e / e n_e$, where η is the resistivity, $\mathbf{v}_e$ is the flow velocity of plasma electrons, p_e is the plasma electron thermal pressure, n_e is the plasma electron density and e is the elementary charge. Finally, the magnetic field is derived from the Faraday's law, $\partial \mathbf{B}/\partial t = -\nabla \times \mathbf{E}$. As only a part of Maxwell's equations needs to be solved, this method is of high speed, which is useful for large scale simulations.

The simulations are based on a ZY Cartesian geometry with the beam propagating along the Z direction. The grid size is 0.1 μm $\times$ 0.2 μm, and the time step is 1.6 fs. To make the proton beam possess a wide energy spectrum similar to the results obtained by the experiments, we set both the kinetic energy and the temperature of the proton beam to 1 MeV. The proton mass density distributions and the electric field distributions are displayed in Fig. 2. By comparing Fig. 2 (a) and (b), we can see that for the boron solid, the proton beam can only penetrate to the surface, whereas for the boron plasma, it can penetrate to a longer distance. Fig. 2 (c) and (d) show that the maximum value of the electric field in the boron solid can reach about 800 GV/m, which is nearly 100 times stronger than in the boron plasma. This is revealed by the fact that the boron solid has a large resistivity, while the boron plasma, with abundant ionized electrons, has a much lower resistivity. Therefore, according to the Ohm's law, the electric field in the boron solid should be much larger.

The energy spectra of α particles escaping from the left simulation boundary in the range of 0 MeV to 6.5 MeV are plotted in Fig. 3. By comparing the blue solid line (N-noEB) and the red solid line (5N-noEB), we find that there are about 40% more α particles produced by the p^{11}B fusion reactions in the laser-ablated boron solid (boron plasma). This can be explained by degeneracy effects, since collisions are suppressed due to the Pauli exclusion principle. Consequantly, the energy loss of the proton beam caused by collisions will be reduced and meanwhile the number of fusion reactions will be enhanced. Nonetheless, degeneracy effects on the yield of α particles can only bring about a 40% gap between the boron solid and the boron plasma. This means they are not the primary factor that causes the large difference found in the experiment.

By comparing the blue solid line (N-noEB) and the blue triangle solid line (N-EB), we can see that there is a large gap in the spectra of α particles, which indicates in terms of the boron solid, the electromagnetic fields have a huge influence on the number of fusion reactions and the yield of α particles. This is because if the electromagnetic fields are not considered, the energy loss of the proton beam is only caused by collisions, whereas if the electromagnetic fields are considered, the energy loss of the proton beam includes both collisions and collective electromagnetic effects. As analyzed above and shown in Fig. 2 (c), when the proton beam is injected into the boron solid, a strong stopping electric field will be generated. It can greatly increase the energy loss of the proton beam and prevent the beam from penetrating. In this way, the number of fusion reactions and the yield of α particles will be decreased. As for the boron plasma, the gap between the red solid line (5N-noEB) and the red square solid line (5N-EB) is not that large because compared with the boron solid, the boron plasma has a lower resistivity and the generated electric field will also be smaller. Therefore, the collectic electromagnetic effects in the boron plasma are not as significant as in the boron solid.

By comparing the blue triangle solid line (N-EB) and the red square solid line (5N-EB), we can see in these two

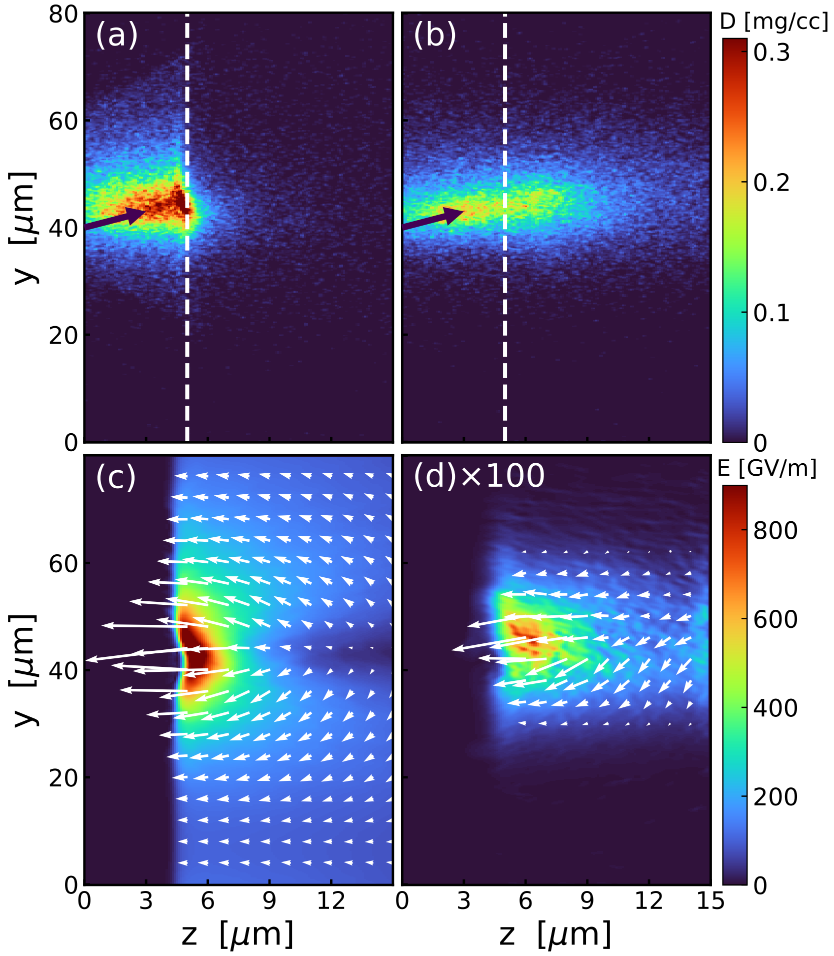

Fig. 2: Mass density distributions of the proton beam and the electric field distributions for the normal boron solid in (a) and (c), and for the laser-ablated boron solid (boron plasma) in (b) and (d), respectively. The boron targets are located on the right side of the white dashed lines in (a) and (b). The black arrows in (a) and (b) indicate the incident direction of the proton beams, of which the angle is 45 degrees to the z axis. The white arrows in (c) and (d) indicate the directions of the electric fields. In (d), the white '×100' means the electric field is magnified by a factor of 100.

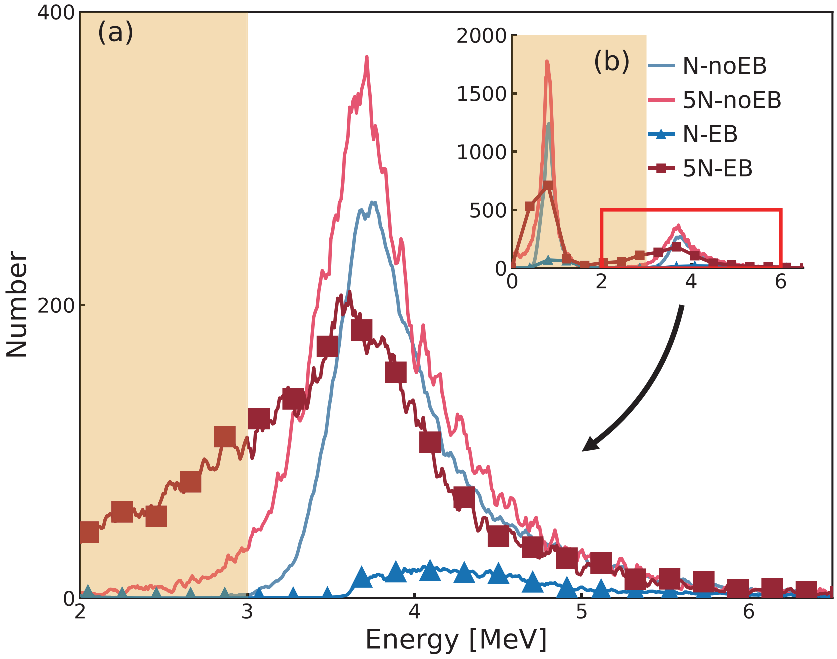

Fig. 3: The energy spectra of α particles escaping from the left simulation boundary in the range of 0 MeV to 6.5 MeV: (1) the blue solid line, boron solid without electromagnetic fields; (2) the red solid line, boron plasma without electromagnetic fields; (3) the blue triangle solid line, boron solid with electromagnetic fields; (4) the red square solid line, boron plasma with electromagnetic fields. The yellow patch corresponds to where cannot be measured in the experiment

cases, the difference in the yields of α particles is close to two orders of magnitude, which is in good agreement with the results at dt= 1.2 ns in the experiments. As we have discussed above, the difference in the yields of α particles actually originates from two aspects: degeneracy effects and collective electromagnetic effects. They exert influences on the number of fusion reactions through changing the energy loss of the proton beam. To be specific, the more energy the proton beam loses during its transport in the boron target, the smaller the number of fusion reactions between protons and boron atomic nuclei and α particles will be.

In conclusion, we have performed a set of simulations on the laser-boron interaction and the p^{11}B fusion reaction by using an intense proton beam to impact boron targets. It is found that after ablation of an intense nanosecond laser, the boron solid turns into a degenerate state at the surface, and quantum degeneracy effects need to be considered. What's more, while a proton beam is propagating in a boron solid, a strong stopping electric field will be generated due to the high resistivity of the boron solid. Degeneracy effects and collective electromagnetic effects will exert influences on the number of fusion reactions through changing the energy loss of the proton beam. By comparing these two effects, we find that collective electromagnetic effects play the dominant role in the p^{11}B fusion reaction and the yields of α particles, and degeneracy effects play a secondary role. Our results may be able to serve as a reference for not only analyzing or improving further experiments of the p^{11}B fusion reaction, but also investigating other beam-plasma systems such as ion-driven inertial confinement fusion and fast ignition.

2 Methods

To make the simulations more credible and closer to the real experimental situation, modules of collisional effects [13], quantum degeneracy effects [14] and nuclear reactions [15] are contained in the LAPINS code. Here, we will briefly describe the physical models used for these modules.

2.1 Collisional effects

The model used in the LAPINS code to deal with collisional effects is based on Monte Carlo binary collisions, which includes binary collisions among electron-electron, electron-ion, and ion-ion and considers contributions from both free and bound electrons. Physical quantities, such as angular scattering, momentum transferring and temperature variation, can be taken into account quite readily in the approach.

In the calculations, three steps are made iteratively: (i) pair of particles are selected randomly in the cell, i.e., either electronelectron, electronion, or ionion pairs; (ii) for these pair of particles, the binary collisions are associated with changes in the velocity of the particles within the time interval δt, which are calculated; (iii) and then the velocity of each particle is replaced by the newly calculated one.

In order to contain both bound and free electrons contribution into the binary collision model, we here take the collision frequency between ions and electrons, in the above (ii) step, as,

$$\nu_{\mathrm{i-e}} = \frac{8\sqrt{2\pi}e^4 Z_b^2 Z n_i}{3m_e^2\beta^3}[\ln(\Lambda_{\mathrm{f}}) + \frac{\mathrm{A-Z}}{\mathrm{Z}}\ln(\Lambda_{\mathrm{b}})], \tag{1}$$

where

$$\ln(\Lambda_{\mathrm{b}}) \equiv \ln[\frac{2\gamma^2 m_e\beta^2}{\bar{I}_A(Z)}] - \beta^2 - C_{\mathrm{K}}/A - \delta/2, \tag{2}$$

and

$$\ln(\Lambda_{\mathrm{f}}) \equiv \ln(\lambda_{\mathrm{D}}/\mathrm{b}). \tag{3}$$

A is the atomic number of stopping medium, Z is the ionization degree of background plasmas, n_i is the nucleus density of stopping medium, m_e is the electron mass, γ is the relativistic factor of the projected ions, β is the velocity of projected ions, $\bar{I}_A$ is the average ionization potential, and Z_b is the effective charge state of injected ion beams, which equals to '1' for the case of protons in our present studies. In Eq. (1), the latter two terms are the shell correction term and the density effect correction term, respectively. These two terms are based on Fano's original work [17], to which the definitions of C_{K}/A and $\delta/2$ can be referred. The Debye length, λ_{D}, is a dynamic value changing as $\lambda_{\mathrm{D}} = \sqrt{(T_e/4\pi n_e)(1+\beta^2/v_{\mathrm{th}}^2)}$, where T_e and v_{th} are the temperature and thermal velocity of background electrons. Parameter b is the distance of closest approach between the two charges. Especially, $(A-Z)/Z$ defines the ratio of bound electrons' contributions. For fully ionized plasmas, $Z \to A$, the collision frequency between ions and electrons converges to

$$\nu_{\mathrm{i-e}} \sim \frac{8\sqrt{2\pi}Z_b^2 e^4 Z n_i}{3m_e^2\beta^3}\ln(\Lambda_{\mathrm{f}}). \tag{4}$$

For neutral atoms, $Z \to 0$, in contrast, the collision frequency is

$$\nu_{\mathrm{i-e}} \sim \frac{8\sqrt{2\pi}Z_b^2 e^4 A n_i}{3m_e^2\beta^3}\ln(\Lambda_{\mathrm{b}}). \tag{5}$$

At the low-temperature limit, when all electrons are bound at the nucleus, the calculated stopping powers converge to the National Institute of Standard and Technology (NIST) ones with the average ionization degree approaching zero as the stopping powers of cold materials can be well calculated by BetheBloch formula. Then, taking advantage of this Monte Carlo binary collision model, we can obtain resistivity η by averaging over all binary collisions at each time step for each simulation cell in a natural manner.

2.2 Degeneracy effects

The model used in the LAPINS code to deal with degeneracy effects is based on the first principle Boltzmann-Uhling-Uhlenbeck (BUU) equation,

$$\frac{\partial f_k}{\partial t} + \mathbf{u}_k \cdot \frac{\partial f_k}{\partial \mathbf{r}} + q_k(\mathbf{E} + \mathbf{u}_k \times \mathbf{B}) \cdot \frac{\partial f_k}{\partial \mathbf{p}_k} = \frac{\partial f_k}{\partial t}|_{\mathrm{coll}}^{\mathrm{BUU}}, \tag{6}$$

where the subscript k indicates the species of particles, $f_k = f_k(\mathbf{r}, \mathbf{p}, t)$ is the distribution function, $\mathbf{r}$ is the position, $\mathbf{p}$ is the momentum, t is the time, $\mathbf{u}$ is the velocity, $\mathbf{E}$ is the electric field, $\mathbf{B}$ is the magnetic field and $\frac{\partial f_k}{\partial t}|_{\mathrm{coll}}^{\mathrm{BUU}}$ is the BUU collision term which can be written as

$$\frac{\partial f_k}{\partial t}|_{\mathrm{coll}}^{\mathrm{BUU}} = \int d^3p_2 \int d^3p_3 \int d^3p_4 W(\mathbf{p}_1, \mathbf{p}_2; \mathbf{p}_3, \mathbf{p}_4) \times (f_{1,2}^{\mathrm{out}} f_{3,4}^{\mathrm{in}} - f_{1,2}^{\mathrm{in}} f_{3,4}^{\mathrm{out}}), \tag{7}$$

where $f_{ij}^{\mathrm{in}} = f_i f_j$, $f_{kl}^{\mathrm{out}} = (1 - f_k)(1 - f_l)$, and $W(\mathbf{p}_1, \mathbf{p}_2; \mathbf{p}_3, \mathbf{p}_4)$ is the collision rate. BUU collisions can ensure that evolution of degererate particles is enforced by the Pauli exclusion principle. This principle prevents degenerate particles being scattering into an energy state if that state is already occupied. For degenerate electrons, under thermal equilibruim, the solution of the BUU equation is a Fermi-Dirac (FD) function,

$$f_e(E) = \frac{(2m_e)^{3/2}}{2n_e\hbar^3\pi^2}\frac{\sqrt{E}}{\exp(E/T_e - \eta) + 1}, \tag{8}$$

where η is the degeneracy parameter and $f_e(E)dE$ is the probability for finding electrons with energy between E and $E + dE$. Degeneracy parameter η can be obtained by equation normalization,

$$\int \frac{(2m_e)^{3/2}}{2n_e\hbar^3\pi^2}\frac{\sqrt{E}dE}{\exp(E/T_e - \eta) + 1} = 1. \tag{9}$$

Here, Eq. (9) defines η as a function of n_e and T_e. When increasing temperature and decreasing density, we have $\eta = -\infty$. This is the classical limit in which the distribution functions become Maxwell-Boltzmann distributions. In the low temperature and high density limit, we have $\eta = E_F/T_e$ and $\eta = \infty$, with $E_F = (3\pi^2 n_e)^{2/3}\hbar^2/2m_e$ of the Fermi energy. This is the fully degenerate limit, in which all particles are at energies below or equal to the Fermi energy.

2.3 Nuclear reactions

The model used to deal with nuclear reactions is based on a pairwise nuclear fusion algorithm for weighted particles at relativistic energies. To simplify algebraic expressions, we might as well set the light speed $c = 1$. For relativistic energies, we treat the kinematics of a relativistic nuclear fusion between two particles with rest masses m_a and m_b, and reduced momenta $\mathbf{u}_a = \gamma_a \mathbf{v}_a$ and $\mathbf{u}_b = \gamma_b \mathbf{v}_b$ in the center-of-momentum frame of reference (CM). The velocity and relativistic factor of CM are

$$\mathbf{v}_{\mathrm{CM}} = \frac{m_a \mathbf{u}_a + m_b \mathbf{u}_b}{m_a \gamma_a + m_b \gamma_b} \tag{10}$$

and

$$\gamma_{\mathrm{CM}} = \frac{1}{(1 - \mathbf{v}_{\mathrm{CM}}^2)^{1/2}}. \tag{11}$$

The reduced momenta $\mathbf{u}_{a,b}$ in the laboratory frame of reference (LAB) are then transformed into the CM frame through a Lorentz transformation

$$\gamma_{a,\mathrm{CM}} = \gamma_{\mathrm{CM}}(\gamma_a - \mathbf{v}_{\mathrm{CM}} \cdot \mathbf{u}_a) \tag{12}$$

and

$$\mathbf{u}_{a,\mathrm{CM}} = \mathbf{u}_a + \frac{\gamma_{\mathrm{CM}} - 1}{\mathrm{v}_{\mathrm{CM}}^2}(\mathbf{v}_{\mathrm{CM}} \cdot \mathbf{u}_a)\mathbf{v}_{\mathrm{CM}} - \gamma_{\mathrm{CM}}\gamma_a \mathbf{v}_{\mathrm{CM}}. \tag{13}$$

The velocities in the CM frame are $\mathbf{v}_{a,\mathrm{CM}} = \mathbf{u}_{a,\mathrm{CM}}/\gamma_{a,\mathrm{CM}}$ and $\mathbf{v}_{b,\mathrm{CM}} = \mathbf{u}_{b,\mathrm{CM}}/\gamma_{b,\mathrm{CM}}$. For the calculation convenience of fusion productions, the coordinate system of momentum space is rotated, in which the $u_{a,z,\mathrm{CM}}$ is the aligned with $\mathbf{u}_{a,\mathrm{CM}}$ and the transformation matrix can be represented by

$$\mathbf{R} = \begin{bmatrix} \cos(\Theta)\cos(\Phi) & \cos(\Theta)\sin(\Phi) & -\sin(\Phi) \\ -\sin(\Phi) & \cos(\Phi) & 0 \\ \sin(\Theta)\cos(\Phi) & \sin(\Theta)\cos(\Phi) & \cos(\Theta) \end{bmatrix} \tag{14}$$

and $[0, 0, u_{a,z,\mathrm{CM}}]^T = \mathbf{R} \cdot [u_{a,x,\mathrm{CM}}, u_{a,y,\mathrm{CM}}, u_{a,z,\mathrm{CM}}]^{\mathrm{T}}$. Here, Θ is the polar angle between $u_{a,z,\mathrm{CM}}$ and $\mathbf{u}_{a,\mathrm{CM}}$, and Φ is the azimuthal angle between $u_{a,x,\mathrm{CM}}$ and $u_{a,y,\mathrm{CM}}$.

The two fusion reactant macro-particles, a and b, have the potential to undergo fusion and create two products,

$\bar{c}$ and $\bar{d}$, with an energy gain, Q. The fusion probability for this interaction, P_{ab}, in the CM frame, is given by

$$\mathrm{P}_{ab} = n_{\min}\sigma_{ab}\mathrm{v}_{\mathrm{rel,CM}}\gamma_{\mathrm{CM}}\Delta t, \tag{15}$$

where $n_{\min}$ is the minimum density between particles species a and b, σ_{ab} is the cross section of nuclear fusion, and Δt is the time step of simulation, which is increased by a factor of γ_{CM} when considered in the CM frame. The relative velocity between the two particles in the CM frame, required for the calculation of the cross section of nuclear fusion, is given by

$$\mathrm{v}_{\mathrm{rel,CM}} = |\frac{\mathbf{v}_{a,\mathrm{CM}} - \mathbf{v}_{b,\mathrm{CM}}}{1 - \mathbf{v}_{a,\mathrm{CM}} \cdot \mathbf{v}_{b,\mathrm{CM}}}|. \tag{16}$$

In general, theoretical and fitted values of the cross sections usually present data using the kinetic energy in the CM frame, $E_r = m_r(\gamma_r - 1)$, where $m_r = m_a m_b/(m_a + m_b)$, and $\gamma_r = 1/(1 - v_{\mathrm{rel}}^2)^{1/2}$. While experimentally, the cross section is usually tabulated as a function of the kinetic energy of the projectile, $E_{a,\mathrm{lab}}$, with $E_{a,\mathrm{lab}} = (m_a + m_b)E_r/m_b$. The nuclear fusion yield for each pair of macro-particles is

$$\mathrm{Y}_{ab} = \omega_{\min}\mathrm{P}_{ab}, \tag{17}$$

where $\omega_{\min}$ is the minimum weight of macro-particles a and b. To increase the number of macro-products generated, Higginson *et al* [18] introduced the "fusion production multiplier" $\mathrm{F}_{\mathrm{multi}}$. This factor increases the probability of fusion events but decreases the weight of the products. In actual simulations, $\mathrm{F}_{\mathrm{multi}}$ is a varying parameter, which depends on how many fusion produced macro-particles are required for data analysis.

The number density of each species within a computational cell can be given with

$$n_a = \sum_{i}^{N_a} \omega_{a,i},\ n_b = \sum_{j}^{N_b} \omega_{b,j}, \tag{18}$$

where $\omega_{a,i}$ is the weight of the ith particle for species of a, and $\omega_{b,j}$ is the weight of the jth particle for species of b. When the number of macro-particles for species of a is larger than that of b, $N_a > N_b$, the number of binary pairs equals to N_a, and the number of binary pairs for real particles equals to

$$n_{ab} = \sum_{i}^{N_a} \frac{\omega_{a,i}\omega_{b,i}}{\max(\omega_{a,i}\omega_{b,i})}. \tag{19}$$

In order to make the total number of binary pairs of real particles equal to the pairs when the particles are uniformly weighted, the time step in Eq. 15 should be corrected with a factor n_a/n_{ab}. Fusion products are produced in the CM frame, with the conservation of total energy and momenta. Since all of the products have the same weight, i.e., $\omega_{\min}/\mathrm{F}_{\mathrm{multi}}$, the fusion process will conserve total energy and momenta perfectly. Here, as the total energy includes the rest mass energy of particles, the kinetic energy, $E_{k,\mathrm{CM}}$, is not conserved, when the rest mass energy is converted into kinetic energy, $E_{k,a,\mathrm{CM}} + E_{k,b,\mathrm{CM}} + Q = E_{k,\bar{c},\mathrm{CM}} + E_{k,\bar{d},\mathrm{CM}}$. For non-relativistic energies, we have

$$P_{\bar{c},\mathrm{CM}}^2 = m_{\bar{c}}^2 u_{\bar{c},\mathrm{CM}}^2 = \frac{2m_{\bar{c}} m_{\bar{d}}}{m_{\bar{c}} + m_{\bar{d}}}[m_r(\gamma_r - 1) + Q], \tag{20}$$

where $m_r(\gamma_r - 1)$ is the total kinetic energy of a and b in the CM frame, and for relativistic energies, as we have $P_{\bar{c},\mathrm{CM}}^2 = (E_{k,\bar{c},\mathrm{CM}} + m_{\bar{c}})^2 - m_{\bar{c}}^2$ and $P_{\bar{c},\mathrm{CM}}^2 = P_{\bar{d},\mathrm{CM}}^2$, the kinetic energy of fusion production $\bar{c}$ is

$$E_{k,\bar{c},\mathrm{CM}} = \frac{1}{2} \frac{(E_{k,a,\mathrm{CM}} + E_{k,b,\mathrm{CM}} + Q + m_{\bar{d}})^2}{(E_{k,a,\mathrm{CM}} + E_{k,b,\mathrm{CM}} + Q + m_{\bar{c}} + m_{\bar{d}})}. \tag{21}$$

Besides, we treat the emission of particles as isotropic with respect to the polar angle, θ, in the CM frame. Either way, the azimuthal angle ϕ is calculated as $\phi = 2\pi u$, with u uniformly distributed number between 0 and 1. These angles are applied to the first product, $\bar{c}$, to get its velocity in the CM frame,

$$\frac{\mathbf{u}_{\bar{c},\mathrm{CM}}}{u_{\bar{c},\mathrm{CM}}} = [\sin(\theta)\cos(\phi), \sin(\theta)\sin(\phi), \cos(\theta)]^{\mathrm{T}}. \tag{22}$$

From momenta conservation, the velocity of the second product, $\bar{d}$, in the CM frame is

$$\mathbf{u}_{\bar{d},\mathrm{CM}} = -\frac{m_{\bar{c}}}{m_{\bar{d}}} \mathbf{u}_{\bar{c},\mathrm{CM}}. \tag{23}$$

Then, we invert the matrix, $\mathbf{R}^{-1}$, which is the transpose of matrix Eq. 14, to obtain the un-rorated momenta in the CM frame, $\mathbf{u}_{\bar{c},\mathrm{CM}} = \mathbf{R}^{-1}\mathbf{u}_{\bar{c},\mathrm{CM}}$ and $\mathbf{u}_{\bar{d},\mathrm{CM}} = \mathbf{R}^{-1}\mathbf{u}_{\bar{d},\mathrm{CM}}$. Finally, the particle momenta $\mathbf{u}_{\bar{c}}$ and $\mathbf{u}_{\bar{d}}$ in the laboratory frame are therefore obtained by another Lorentz transformation. Such calculations will be performed for each binary pair in each computation cell.

3 Acknowledgments

This work was supported by the National Natural Science Foundation of China (Grant Nos.11875235, 61627901 and 12075204), the Strategic Priority Research Program of Chinese Academy of Sciences (Grant No. XDA250050500), and We thank Dr. Jinlong Jiao for his help in the radiation hydrodynamics simulations with the MULTI-1D code.

References

[1] B.N. Wan, Y.F. Liang, X.Z. Gong, J.G. Li, N. Xiang, G.S. Xu, Y.W. Sun, L. Wang, J.P. Qian, H.Q. Liu, X.D. Zhang, L.Q. Hu, J.S. Hu, F.K. Liu, C.D. Hu, Y.P. Zhao, L. Zeng, M. Wang, H.D. Xu, G.N. Luo, A.M. Garofalo, A. Ekedahl, L. Zhang, X.J. Zhang, J. Huang, B.J. Ding, Q. Zang, M.H. Li, F. Ding, S.Y. Ding, B. Lyu, Y.W. Yu, T. Zhang, Y. Zhang, G.Q. Li, T.Y. Xia, and and. Overview of EAST experiments on the development of high-performance steady-state scenario. *Nucl. Fusion*, 57:102019, 2017.

[2] D. Clery. Laser-powered fusion effort nears 'ignition'. *Science*, 373:841, 2021.

[3] V. S. Belyaev, A. P. Matafonov, V. I. Vinogradov, V. P. Krainov, V. S. Lisitsa, A. S. Roussetski, G. N. Ignatyev, and V. P. Andrianov. Observation of neutronless fusion reactions in picosecond laser plasmas. *Phys. Rev. E*, 72:026406, 2005.

[4] C. Labaune, C. Baccou, S. Depierreux, C. Goyon, G. Loisel, V. Yahia, and J. Rafelski. Fusion reactions initiated by laser-accelerated particle beams in a laser-produced plasma. *Nat. Commun.*, 4:2506, 2013.

[5] A. Picciotto, D. Margarone, A. Velyhan, P. Bellutti, J. Krasa, A. Szydlowsky, G. Bertuccio, Y. Shi, A. Mangione, J. Prokupek, A. Malinowska, E. Krousky, J. Ullschmied, L. Laska, M. Kucharik, and G. Korn. Boron-proton nuclear-fusion enhancement induced in boron-doped silicon targets by low-contrast pulsed laser. *Phys. Rev. X*, 4:031030, 2014.

[6] C. Baccou, S. Depierreux, V. Yahia, C. Neuville, C. Goyon, R. De Angelis, F. Consoli, J. E. Ducret, G. Boutoux, J. Rafelski, and C. Labaune. New scheme to produce aneutronic fusion reactions by laser-accelerated ions. *Laser and Particle Beams*, 33:117–122, 2015.

[7] L. Giuffrida, F. Belloni, D. Margarone, G. Petringa, G. Milluzzo, V. Scuderi, A. Velyhan, M. Rosinski, A. Picciotto, M. Kucharik, J. Dostal, R. Dudzak, J. Krasa, V. Istokskaia, R. Catalano, S. Tudisco, C. Verona, K. Jungwirth, P. Bellutti, G. Korn, and G. A. P. Cirrone. High-current stream of energetic alpha particles from laser-driven proton-boron fusion. *Phys. Rev. E*, 101:013204, 2020.

[8] Daniele Margarone, Alessio Morace, Julien Bonvalet, Yuki Abe, Vasiliki Kantarelou, Didier Raffestin, Lorenzo Giuffrida, Philippe Nicolai, Marco Tosca, Antonino Picciotto, Giada Petringa, Giuseppe A. P. Cirrone, Yuji Fukuda, Yasuhiro Kuramitsu, Hideaki Habara, Yasunobu Arikawa, Shinsuke Fujioka, Emmanuel D'Humieres, Georg Korn, and Dimitri Batani. Generation of α-particle beams with a multi-kj, peta-watt class laser system. *Frontiers in Physics*, 8:343, 2020.

[9] J. Bonvalet, P. Nicolai, D. Raffestin, E. D'Humieres, D. Batani, V. Tikhonchuk, V. Kantarelou, L. Giuffrida, M. Tosca, G. Korn, A. Picciotto, A. Morace, Y. Abe, Y. Arikawa, S. Fujioka, Y. Fukuda, Y. Kuramitsu, H. Habara, and D. Margarone. Energetic alpha-particle sources produced through proton-boron reactions by high-energy high-intensity laser beams. *Phys. Rev. E*, 103:053202, 2021.

[10] S. Kimura, A. Anzalone, and A. Bonasera. Comment on "observation of neutronless fusion reactions in picosecond laser plasmas". *Phys Rev E Stat Nonlin Soft Matter Phys*, 79:038401, 2009.

[11] F. Y. Wu, R. Ramis, Z. H. Li, Y. Y. Chu, J. L. Yang, Z. Wang, S. J. Meng, Z. C. Huang, and J. M. Ning. Numerical simulation of the interaction between z-pinch plasma and foam converter using code multi. *Fusion Sci. Technol.* $72, 726$ (2017).

[12] D. Wu, W. Yu, S. Fritzsche, and X. T. He. High-order implicit particle-in-cell method for plasma simulations at solid densities. *Phys. Rev. E* $100, 013207$ (2019).

[13] D. Wu, X. T. He, W. Yu, and S. Fritzsche. Monte carlo approach to calculate proton stopping in warm dense matter within particle-in-cell simulations. *Phys. Rev. E* $95, 023207$ (2017).

[14] D. Wu, W. Yu, S. Fritzsche, and X. T. He. Particle-in-cell simulation method for macroscopic degenerate plasmas. *Phys. Rev. E* 102, 033312 (2020).

[15] D. Wu, Z. M. Sheng, W. Yu, S. Fritzsche, and X. T. He. A pairwise nuclear fusion algorithm for particle-in-cell simulations: Weighted particles at relativistic energies. *AIP Advances* 11, 075003 (2021).

[16] D. Wu, W. Yu, Y. T. Zhao, D. H. H. Hoffmann, S. Fritzsche, and X. T. He. Particle-in-cell simulation of transport and energy deposition of intense proton beams in solid-state materials. *Phys. Rev. E* 100, 013208 (2019).

[17] U. Fano. Penetration of protons, alpha particles, and mesons. *Annu. Rev. Nucl. Sci.* 13, 1 − 66 (1963).

[18] Drew Pitney Higginson, Anthony Link, and Andrea Schmidt. A pairwise nuclear fusion algorithm for weighted particle-in-cell plasma simulations. *Journal of Computational Physics*, 388:439–453, 2019.